

Scale-dependent bias and mode coupling in redshift-space clustering near the BAO scale

Aseem Paranjape^a and Ravi K. Sheth^{b,c}

^aInter-University Centre for Astronomy & Astrophysics,
Ganeshkhind, Post Bag 4, Pune 411007, India

^bCenter for Particle Cosmology, University of Pennsylvania,
209 S. 33rd St., Philadelphia, PA 19104, USA

^cThe Abdus Salam International Center for Theoretical Physics,
Strada Costiera, 11, Trieste 34151, Italy

E-mail: aseem@iucaa.in, shethrk@physics.upenn.edu

Abstract. The baryon acoustic oscillation (BAO) feature in the 2-point clustering of biased tracers in redshift space can be described in a model-agnostic manner, relying only on the assumption that nonlinear growth approximately smears this feature with a Gaussian kernel sourced by gravitationally driven bulk flows as in the Zel'dovich approximation. An explicit model that demonstrated this in recent work did not account for two physical effects that are very likely observationally relevant in the context of ongoing surveys, namely, the scale-dependence of linear Lagrangian density and velocity bias and the effects of mode coupling. We rectify this shortcoming in this paper by showing that a simple model including these effects is able to accurately describe the multipoles of the 2pcf of realistic tracer samples at BAO scales. Our results indicate that the effects of scale-dependent bias will be important to model for surveys such as DESI, while those of mode coupling are relatively less significant. Our model for scale-dependent bias and mode coupling, which is motivated by model-agnostic arguments from peaks theory and the Zel'dovich approximation, lies in the class of ‘Laplace-Gauss’ expansions, making it straightforward to incorporate these effects in the model-agnostic inference framework mentioned above.

Keywords: baryon acoustic oscillations, galaxy clustering.

Contents

1	Introduction	1
2	Model	2
2.1	Smearing due to displacements	2
2.2	Modelling scale-dependent bias	3
2.3	Modelling mode coupling	5
2.4	Configuration space multipoles	6
3	Simulations and Analysis	6
3.1	Simulations	6
3.2	Gauss-Poisson covariance matrix	7
4	Results	8
4.1	Base model	8
4.2	Model variations	11
4.2.1	Scale-dependent bias	11
4.2.2	Mode coupling	11
5	Conclusion	12
A	Fourier space results	16
B	Accuracy and generality of our treatment of mode coupling	20

1 Introduction

The baryon acoustic oscillation (BAO) feature in the clustering of biased tracers such as galaxies is one of the primary science drivers in current, upcoming and planned surveys of large-scale structure [1–5]. This is not only from the viewpoint of increasingly precise constraints on parameters in the Lambda-cold dark matter (Λ CDM) model, but also in the hunt for signatures of departures from the standard model [6–8]. Traditional methods [9–15] exploit the information content of the BAO feature in 2-point clustering (in configuration or Fourier space) by assuming templates based on a fiducial Λ CDM model and constraining parameters describing variations around this model. Field-level inference techniques are now being explored to maximise information recovery from the BAO feature within Λ CDM [16, 17]. Recent work has also shown how this information might be repackaged in model-agnostic analyses that do not rely on Λ CDM templates [18–23].

In a recent work [24, hereafter, PS23], we showed how the shape of the BAO feature in redshift space, as characterised by the multipoles of the 2-point correlation function (2pcf) of galaxies, can be described by a model that *does not* assume the Λ CDM framework. Rather, we assume that the Zel'dovich approximation is a good description of the nonlinear motion of matter at large scales. In this case, the BAO feature is smeared by an approximately Gaussian kernel [25, 26] whose width σ_v is a parameter of cosmological interest. PS23 showed that this model (which we recapitulate below) can successfully describe the clustering of galaxies in

existing surveys and provide meaningful constraints on σ_v as well as the linear growth rate f , *without* assuming a Λ CDM cosmology. However, the model as stated in [PS23](#) was unable to accurately recover these parameters when making projections for ongoing surveys such as the one by the Dark Energy Spectroscopic Instrument (DESI) collaboration [\[27\]](#). This is particularly relevant in the context of the recent early results from DESI hinting at possible departures from the standard model [\[28\]](#).

Our aim in the present work is to improve upon the [PS23](#) model by rectifying two of its main shortcomings, namely, the lack of scale-dependence of the bias of the underlying tracers and the lack of mode coupling effects expected due to nonlinear growth. On BAO scales, the former is expected to be more important than the latter [\[29, 30\]](#). Nevertheless, we will show that both of these effects can be incorporated into an extension of the [PS23](#) model adding only minimal assumptions: (a) that the distribution and motion of point tracers such as galaxies is modified compared to the matter distribution along the lines suggested by peaks theory, and (b) that, on BAO scales, the dominant contribution to the mode-coupling effect comes from a dipole-like contribution whose form is constrained by Galilean invariance [\[31\]](#). Our focus in this paper is to demonstrate that our resulting model of redshift space multipoles of the 2pcf including scale-dependent bias and mode coupling provides an accurate description of measurements of these quantities in Λ CDM simulations for realistic tracer populations. We leave the application of our setup in a full model-agnostic inference exercise to a forthcoming publication.

The paper is structured as follows. In section 2 we recapitulate the model from [PS23](#) and then describe our modifications to include the effects of scale-dependent bias and mode coupling. We describe the simulations we use, along with our analysis for validating the model, in section 3. Section 4 presents our results for the base model we propose in this work, and also reports the results of variations around this model as a means of testing its robustness. We conclude in section 5. Although built using Fourier space ingredients, our model is intended to be accurate at large scales in configuration space. As a sanity check, however, in Appendix A we also study its accuracy in Fourier space at low values of wavenumber k .

2 Model

Our starting point is a description of the non-linear clustering of biased tracers near the BAO feature in redshift space that is motivated by the Zel'dovich approximation written in the language of renormalized perturbation theory [\[26, 32, 33\]](#). Here, one writes the non-linearly evolved galaxy 2pcf in redshift space, $\xi_{\text{NL}}(\mathbf{s})$, as a sum of two contributions,

$$\xi_{\text{NL}}(\mathbf{s}) = \xi_{\text{prop}}(\mathbf{s}) + \xi_{\text{MC}}(\mathbf{s}), \quad (2.1)$$

where the ‘propagator’ term $\xi_{\text{prop}}(\mathbf{s})$ accounts for the effect of bulk flows on the large-scale tracer correlations, while the mode coupling term $\xi_{\text{MC}}(\mathbf{s})$ additionally accounts for nonlinearities at smaller scales. [PS23](#) discussed a simple model for $\xi_{\text{prop}}(\mathbf{s})$ (which we recapitulate below) and ignored $\xi_{\text{MC}}(\mathbf{s})$. Below, we extend their model to account for the effects of, both, scale-dependent bias and mode coupling. In particular, we argue that the mode coupling term $\xi_{\text{MC}}(\mathbf{s})$ is expected to be related to the propagator term $\xi_{\text{prop}}(\mathbf{s})$.

2.1 Smearing due to displacements

If $\xi_L(\mathbf{s})$ is the linearly evolved galaxy 2pcf in redshift space, and we focus on large separations s close to the BAO feature, then the effect of bulk flows in the propagator term of equation (2.1)

is to smear the linear 2pcf according to [25, 26, 33]

$$\xi_{\text{prop}}(\mathbf{s}) \approx \int d^3s' \xi_L(s') \mathcal{N}(\mathbf{s} - \mathbf{s}'; \boldsymbol{\Sigma}), \quad (2.2)$$

where $\mathcal{N}(\mathbf{x}; \boldsymbol{\Sigma})$ denotes a 3-dimensional Gaussian distribution in \mathbf{x} having zero mean and covariance matrix $\boldsymbol{\Sigma}$. This matrix is anisotropic in redshift space, with variances σ_{\parallel}^2 and σ_{\perp}^2 along and perpendicular to the line-of-sight, respectively, given by [34–36]

$$\sigma_{\parallel}^2 = 2\sigma_v^2(1+f)^2 \quad \text{and} \quad \sigma_{\perp}^2 = 2\sigma_v^2, \quad (2.3)$$

where $f \equiv d \ln D / d \ln a$ is the usual linear growth rate and we defined the linear theory 1-dimensional, single-particle velocity dispersion σ_v

$$\sigma_v^2 \equiv \frac{1}{3} \int d \ln k k^{-2} \Delta_{\text{lin}}^2(k), \quad (2.4)$$

with $\Delta_{\text{lin}}^2(k) = k^3 P_{\text{lin}}(k) / (2\pi^2)$ being the dimensionless linear theory matter power spectrum (whose redshift dependence is suppressed). The large-scale redshift-space 2pcf $\xi_L(\mathbf{s})$ appearing in equation (2.2) is

$$\xi_L(\mathbf{s}) = \int \frac{d^3k}{(2\pi)^3} e^{i\mathbf{k} \cdot \mathbf{s}} b^2 (1 + \beta \mu_k^2)^2 P_{\text{lin}}(k), \quad (2.5)$$

where b is the large-scale Eulerian bias of the sample and $\beta \equiv f/b$ [37].

This gives the expression in equation (17) of PS23 for the non-linear power spectrum multipoles¹ $\Delta_{\text{prop}}^{(\ell)2}$:

$$\Delta_{\text{prop}}^{(\ell)2}(k) = \Delta_{\text{lin}}^2(k) b^2 e^{-k^2 \sigma_v^2} (2\ell + 1) \int_{-1}^1 \frac{d\mu_k}{2} \mathcal{P}_{\ell}(\mu_k) (1 + \beta \mu_k^2)^2 e^{-K^2 \mu_k^2}, \quad (2.6)$$

where

$$K^2 \equiv k^2 \sigma_v^2 f(f+2), \quad (2.7)$$

and $\mathcal{P}_{\ell}(\mu)$ is the Legendre polynomial of degree ℓ . Our goal here is to extend this model to include the effects of scale-dependent density and velocity bias along with mode coupling.

2.2 Modelling scale-dependent bias

To include the effects of scale-dependence of the density and velocity bias at linear order, we make the replacement

$$b + f \mu_k^2 \rightarrow b_{\text{Lag}}(k) + b_{\text{vel}}(k)(1 + f \mu_k^2) \equiv b B(k, \mu_k). \quad (2.8)$$

We discuss our model for $b_{\text{Lag}}(k)$ and $b_{\text{vel}}(k)$ below. Our starting point is the result that, at fixed halo mass m , the Lagrangian linear density and velocity bias factors are very well approximated by the peaks theory form [30, 35, 38]

$$b_{\text{Lag}}(k|m) = [b_{10}(m) + b_{01}(m) k^2 R_{\text{pk}}^2] e^{-k^2 R_{\text{h}}^2/2}, \quad (2.9)$$

$$b_{\text{vel}}(k|m) = [1 - k^2 R_{\text{pk}}^2] e^{-k^2 R_{\text{h}}^2/2}, \quad (2.10)$$

¹PS23 referred to this as their ‘exact’ model for the multipoles of the *full* power spectrum $\Delta_{\text{NL}}^{(\ell)2}$.

where $R_h = (3m/4\pi\bar{\rho})^{1/3}/\sqrt{5}$ is the Lagrangian scale² corresponding to mass m and R_{pk} is the characteristic peaks scale for mass m , given by

$$R_{\text{pk}}(m) \equiv \frac{\sigma_0(R_h)}{\sigma_1(R_h)}, \quad (2.11)$$

where the $z = 0$ spectral integrals $\sigma_j^2(R)$ are given by

$$\sigma_j^2(R) \equiv \int d \ln k \Delta_{\text{lin}}^2(k) k^{2j} e^{-k^2 R^2}. \quad (2.12)$$

In equation (2.9), $b_{10}(m)$ is the peak-background split contribution to linear Lagrangian density bias and $b_{01}(m)$ is related to $b_{10}(m)$ through a consistency relation of the form

$$b_{10}(m) + b_{01}(m) = \frac{\delta_{\text{crit}}(m)}{\sigma_0(R_h)^2}, \quad (2.13)$$

where $\delta_{\text{crit}}(m)$ is the linearly extrapolated critical density for collapse, whose canonical value at $z = 0$ in the spherical collapse model is $\simeq 1.686$, but which can have an effective mass dependence due to effects of non-sphericity [40, 41] or tides [42].

The detailed mass dependence of the factors b_{10} and b_{01} is quite model dependent. Moreover, galaxy samples typically do not correspond to narrow – or even well-defined – ranges of halo mass. In principle, we then need a model that is flexible enough to capture not only the inherent uncertainties in modelling the fixed-mass coefficients above, but also the effects of averaging over halo mass. The structure in equations (2.9)–(2.10) motivates a model for $b_{\text{Lag}}(k)$ and $b_{\text{vel}}(k)$ given by

$$b_{\text{Lag}}(k) = [b - 1 + b_{01}k^2 R_p^2] e^{-k^2 R_*^2/2}, \quad (2.14)$$

$$b_{\text{vel}}(k) = [1 - B_v k^2 R_p^2] e^{-k^2 R_*^2/2}, \quad (2.15)$$

where b_{01} , B_v and R_* are free parameters and R_p is a fixed pivot scale. This in turn leads to the following expression for $B(k, \mu_k)$ (equation 2.8)

$$\begin{aligned} B(k, \mu_k) &= b^{-1} [b - 1 + b_{01}k^2 R_p^2 + (1 - B_v k^2 R_p^2)(1 + f\mu_k^2)] e^{-k^2 R_*^2/2} \\ &= b^{-1} [b + (b_{01} - B_v)R_p^2 k^2 + f\mu_k^2(1 - B_v R_p^2 k^2)] e^{-k^2 R_*^2/2} \\ &\equiv [1 + B_1 k^2 R_p^2 + \beta\mu_k^2 (1 - B_v k^2 R_p^2)] e^{-k^2 R_*^2/2}, \end{aligned} \quad (2.16)$$

where we defined $B_1 \equiv (b_{01} - B_v)/b$. Our model for scale-dependent bias thus has 3 free parameters in addition to the large-scale bias b : R_* represents a characteristic Lagrangian scale of the tracer population, while B_1 and B_v capture the additional peaks-theory-like effects of scale-dependence. The pivot scale R_p only serves to make B_1 and B_v dimensionless; throughout this work we fix its value to $R_p = 2.5h^{-1}\text{Mpc}$. The primary advantage of this model is that it falls within the class of ‘Laplace-Gauss’ expansions discussed by PS23, which allow for straightforward implementations of model-agnostic inference as discussed by those authors. We return to this point in section 5. We will test this model below using redshift-space clustering measurements for mass-thresholded halo samples in N -body simulations of ΛCDM .

²The factor of $\sqrt{5}$ accounts for the fact that the Lagrangian scale is generally associated with a tophat filter in real space, while we are working with Gaussian filters; see the discussion in [39].

2.3 Modelling mode coupling

To model the potentially anisotropic effects of mode coupling (MC), we follow [33, CS08] who argue that the leading order MC effect near the BAO feature in real space is of the form ($\sim d\xi_{\text{lin}}/d\ln r$) $\bar{\xi}_{\text{lin}}$. Further noting that the volume averaged 2pcf $\bar{\xi}_{\text{lin}}$ is featureless and relatively flat across the BAO feature, CS08 motivate modelling the monopole of the redshift space 2pcf of biased tracers by adding a term proportional to $d\xi_{\text{lin}}(s)/d\ln s$ to the 2pcf of our previous Zel'dovich smearing approximation (their equation 34).

We discuss how to extend this to biased, redshift space distorted tracers, and how strongly this depends on ΛCDM , in Appendix B. Importantly, this discussion shows that, similarly to the calculation by CS08 for dark matter, the dominant contribution to the mode coupling term for tracers with scale-dependent bias is *also* expected to be approximately proportional to a derivative of the propagator term. Motivated by this, we consider the following ansatz for $\xi_{\text{NL}}(\mathbf{s})$ that includes anisotropic effects of, both, mode coupling as well as scale-dependent bias:

$$\xi_{\text{NL}}(\mathbf{s}) = \int d^3s' \xi_{\text{L}}(\mathbf{s}'|0) \mathcal{N}(\mathbf{s} - \mathbf{s}'; \boldsymbol{\Sigma}) + A_{\text{MC}} \frac{\partial \xi_{\text{L}}(\mathbf{s}|R_{\text{MC}})}{\partial \ln s}, \quad (2.17)$$

with

$$\xi_{\text{L}}(\mathbf{s}|R) \equiv \int \frac{d^3k}{(2\pi)^3} e^{i\mathbf{k}\cdot\mathbf{s}} b^2 B(k, \mu_k)^2 e^{-k^2 R^2} P_{\text{lin}}(k). \quad (2.18)$$

Note that the expression for $\xi_{\text{L}}(\mathbf{s}|R)$ is different from the one for $\xi_{\text{L}}(\mathbf{s})$ in equation (2.5) not only due to the Gaussian smearing with scale R but also the scale-dependent bias factor $B(k, \mu_k)$. The first integral in equation (2.17) is our model for $\xi_{\text{prop}}(\mathbf{s})$, while the second term is our approximation for $\xi_{\text{MC}}(\mathbf{s})$. Appendix B would actually suggest setting $\xi_{\text{MC}}(\mathbf{s}) = A_{\text{MC}} d\xi_{\text{prop}}(\mathbf{s})/d\ln s$, so that the smearing appearing in this term is anisotropic, being derived from that in $\xi_{\text{prop}}(\mathbf{s})$. There are, however, several approximations made before arriving at this proportionality in Appendix B and, strictly, the pre-factor A_{MC} should also not be a constant. To approximately account for these differences, we have chosen to simplify the ansatz and only use an isotropic smearing when describing $\xi_{\text{MC}}(\mathbf{s})$, while allowing the smearing scale R_{MC} to be a free parameter and not necessarily equal to σ_v (which appears in the anisotropic kernel in $\xi_{\text{prop}}(\mathbf{s})$). We will see below, however, that our comparisons with numerical simulations strongly support setting $R_{\text{MC}} \simeq \sigma_v$ in equation (2.17), which builds confidence in our approximations.

Thus, our model of nonlinear redshift-space clustering including scale-dependent bias and mode coupling, which we refer to as *sdbmc* below, contains 5 free parameters $\{B_1, B_v, A_{\text{MC}}, R_{\text{MC}}, R_*\}$ apart from the large-scale bias b , the velocity dispersion σ_v and the growth rate f . Here, $\{B_1, B_v, R_*\}$ describe the effects of scale-dependent bias and $\{A_{\text{MC}}, R_{\text{MC}}\}$ describe mode coupling. When these 5 parameters are set to zero, the model reduces to the one discussed by PS23, which we refer to as *no sdbmc* below.

Throughout this work, we will set σ_v and f to the values inferred from the appropriate cosmological model, mentioned in section 3.1. In a full-fledged inference exercise, of course, σ_v and f would be left free; we will study this in a forthcoming publication. For simplicity, below we will fix b and R_* to the values inferred from the large-scale clustering and mass distribution of the halo sample and only vary $\{B_1, B_v, A_{\text{MC}}, R_{\text{MC}}\}$. When considering galaxy samples, which need not correspond to well-defined halo mass cuts, the values of b and R_* might also need to be varied, possibly with well-motivated priors (see, e.g., the discussion in PS23 and also below).

2.4 Configuration space multipoles

We will compare this model with 2pcf measurements in configuration space, near the BAO scale, and consequently need the multipole moments of the preceding expressions. A calculation similar to that leading from equation (10) to equation (16) in PS23 gives

$$\xi_{\text{NL}}^{(\ell)}(s) = \xi_{\text{prop}}^{(\ell)}(s) + \xi_{\text{MC}}^{(\ell)}(s), \quad (2.19)$$

where

$$\xi_{\text{prop}}^{(\ell)}(s) = i^\ell \int d \ln k \Delta_{\text{prop}}^{(\ell)2}(k) j_\ell(ks), \quad (2.20)$$

$$\xi_{\text{MC}}^{(\ell)}(s) = A_{\text{MC}} i^\ell \int d \ln k \Delta_{\text{L}}^{(\ell)2}(k) [\ell j_\ell(ks) - ks j_{\ell+1}(ks)], \quad (2.21)$$

with

$$\Delta_{\text{prop}}^{(\ell)2}(k) \equiv \Delta_{\text{lin}}^2(k) b^2 e^{-k^2 \sigma_v^2} (2\ell + 1) \int_{-1}^1 \frac{d\mu_k}{2} \mathcal{P}_\ell(\mu_k) B(k, \mu_k)^2 e^{-K^2 \mu_k^2}, \quad (2.22)$$

$$\Delta_{\text{L}}^{(\ell)2}(k) \equiv \Delta_{\text{lin}}^2(k) b^2 e^{-k^2 R_{\text{MC}}^2} (2\ell + 1) \int_{-1}^1 \frac{d\mu_k}{2} \mathcal{P}_\ell(\mu_k) B(k, \mu_k)^2, \quad (2.23)$$

and we used the identity

$$x d j_\ell(x) / dx = \ell j_\ell(x) - x j_{\ell+1}(x), \quad (2.24)$$

in writing equation (2.21). In the limit of scale independent bias ($B(k, \mu_k) \rightarrow 1 + \beta \mu_k^2$), $\Delta_{\text{prop}}^{(\ell)2}(k)$ reduces to equation (2.6) (i.e., equation (17) of PS23), while $\Delta_{\text{L}}^{(\ell)2}(k)$ reduces to the Kaiser multipoles, $\Delta_{\text{L}}^{(\ell)2}(k) \rightarrow \Delta_{\text{lin}}^2(k) b^2 \chi_\ell(\beta)$. This model can also be compared with multipole measurements in Fourier space; we provide the necessary conversions in Appendix A. In fact, to compute $\xi_{\text{MC}}^{(\ell)}(s)$ in practice, we first evaluate equations (A.11)-(A.13) in Fourier space and then perform an integral over k .

3 Simulations and Analysis

3.1 Simulations

For the results in the main text, we rely on 20 realisations of the HADES N -body simulations [43]. Each run evolved 512^3 particles in a $(1h^{-1}\text{Gpc})^3$ volume using a flat ΛCDM cosmology with parameters $\Omega_m = 0.3175$, $\Omega_b = 0.049$, $h = 0.6711$, $n_s = 0.9624$, $\sigma_8 = 0.833$, with a particle mass of $m_{\text{part}} = 6.56 \times 10^{11} h^{-1} M_\odot$. Specifically, we use mass-weighted³ measurements of the configuration space multipoles of the 2pcf $\hat{\xi}^{(\ell)}$ for $\ell = 0, 2, 4$ presented by [44] using halo catalogs at $z = 0$, with halos identified using the Friends-of-Friends algorithm. The halo sample in each realisation was defined using a mass threshold of $m \geq 20 m_{\text{part}} \simeq 1.3 \times 10^{13} h^{-1} M_\odot$. The combined volume of the 20 HADES realisations is similar to the effective volume of the LRG sample in the DESI survey [27]. The large-scale clustering strength of this sample (see below) is $b \simeq 1.95$, also comparable to that expected for DESI LRGs. The

³Although the mass-weighting was implemented by the authors of [44] to aid their reconstruction analysis, in our case it has the desirable effect of approximating the impact of satellite galaxies in the sample.

effective number density of the sample⁴ is $\bar{n} \simeq 1.1 \times 10^{-4} (h \text{ Mpc}^{-1})^3$, about a factor 6 smaller than the expected DESI LRG density. Note, however, that the HADES measurements are at $z = 0$ while DESI LRGs are expected to lie at $z \sim 0.7$, so a direct comparison cannot be made. The growth factor for this cosmology and redshift is $f = 0.53$, while the linear velocity dispersion is $\sigma_v = 6.0 h^{-1} \text{Mpc}$.

For the results in Appendix A, we rely on the MINERVA N -body simulations described by Grieb *et al.* [45]. These evolved 1000^3 particles in a $(1.5 h^{-1} \text{Gpc})^3$ volume using a flat ΛCDM cosmology with parameters $\Omega_m = 0.285$, $\Omega_b = 0.04606$, $h = 0.695$, $n_s = 0.9632$, $\sigma_8 = 0.828$. Grieb *et al.* further constructed mock galaxy catalogs using a halo occupation distribution (HOD) model in halos identified at $z = 0.57$, designed to mimic the CMASS sample of the BOSS survey [46] and having $b = 2.005$ and $\bar{n} = 4 \times 10^{-4} (h \text{ Mpc}^{-1})^3$. We use the Fourier space measurements of power spectrum multipoles presented in fig. 3 of [45]. The corresponding configuration space measurements are not available to us. The growth factor and linear velocity dispersion for this cosmology and redshift are $f = 0.76$ and $\sigma_v = 4.6 h^{-1} \text{Mpc}$.

3.2 Gauss-Poisson covariance matrix

As in PS23, we work in the Gauss-Poisson approximation, where the covariance matrix

$$C_{ij}^{\ell\ell'} \equiv \left\langle \xi_{\text{NL}}^{(\ell)}(s_i) \xi_{\text{NL}}^{(\ell')}(s_j) \right\rangle - \left\langle \xi_{\text{NL}}^{(\ell)}(s_i) \right\rangle \left\langle \xi_{\text{NL}}^{(\ell')}(s_j) \right\rangle \quad (3.1)$$

can be written as [e.g., 45],

$$C_{ij}^{\ell\ell'} = \frac{i^{\ell_1 + \ell_2}}{2\pi^2} \int dk k^2 \bar{j}_{\ell_1}(ks_i) \bar{j}_{\ell_2}(ks_j) \sigma_{\ell_1 \ell_2}^2(k). \quad (3.2)$$

Here

$$\begin{aligned} \sigma_{\ell_1 \ell_2}^2(k) &= \frac{(2\ell_1 + 1)(2\ell_2 + 1)}{V_{\text{sur}}/2} \\ &\times \int_{-1}^1 \frac{d\mu}{2} \left[P(k, \mu) + \frac{1}{\bar{n}} \right]^2 \mathcal{P}_{\ell_1}(\mu) \mathcal{P}_{\ell_2}(\mu) \end{aligned} \quad (3.3)$$

for a survey of volume V_{sur} with observed tracer number density \bar{n} and

$$\bar{j}_{\ell}(ks_i) = \frac{4\pi}{V_i} \int ds s^2 j_{\ell}(ks) W_i(s) \quad (3.4)$$

with

$$V_i = 4\pi \int ds s^2 W_i(s), \quad (3.5)$$

where $W_i(s)$ describes the shape of a window over which j_{ℓ} has been averaged. E.g., for the tophat bins of width Δs centered on s_i that we use, $W_i(s) = 1$ if $s_i - \Delta s/2 \leq s \leq s_i + \Delta s/2$ and zero otherwise, and the integral which defines \bar{j}_{ℓ} can be done analytically.

⁴Due to mass-weighting, the number density is not simply the ratio of the number of tracers to the box volume V . Rather, it must be calculated using $\bar{n}^{-1} = \sum_i m_i^2/V / (\sum_i m_i/V)^2$, where m_i is the mass of the i^{th} halo and the sum is over all halos in the sample. This leads to $\bar{n}^{-1} \simeq 9000(h^{-1} \text{Mpc})^3$ [e.g., the dashed line in fig. 5 of 44].

For the configuration-space results in the main text, we further scale the Gauss-Poisson covariance matrix so as to maintain its correlation structure while agreeing with the diagonal errors on $\hat{\xi}^{(\ell)}(s)$ from the simulation measurements. For the Fourier space results in Appendix A, we integrate $\sigma_{\ell_1\ell_2}^2(k)$ over appropriate bins in k , rather than the Bessel-weighted integrals in equation (3.3), and use the Gauss-Poisson matrix directly. Neither of these choices significantly impacts our final results or conclusions.

We perform parameter inference using the Monte Carlo Markov Chain (MCMC) technique. Below, we use the publicly available COBAYA [47, 48]⁵ and GETDIST [49]⁶ packages to implement the MCMC and display results, respectively, discarding the first 30% of the samples as burn-in. We assume a Gaussian likelihood throughout. Wherever needed, we generate cosmological transfer functions for matter fluctuations using the CLASS code [50, 51].⁷

4 Results

4.1 Base model

We now attempt to describe the configuration space multipole moment measurements $\hat{\xi}^{(\ell)}(s)$ at $z = 0$ at BAO scales for $\ell = 0, 2, 4$ in the HADES simulations presented by [44], using the *sdbmc* model. In Appendix A, we report the results of a similar exercise to describe the Fourier space multipole measurements reported by [45] in the MINERVA simulations at $z = 0.57$.

As mentioned above, for this exercise we set $R_* = 2.5h^{-1}\text{Mpc}$ to approximately match the characteristic mass of the sample discussed in section 3.1. We have checked that small variations in this value do not affect the details or quality of our fits below. In general, the scale as well as shape of the filter could be varied, e.g., by expanding around a Gaussian shape in powers of k^2 .⁸ To proceed with the analysis, we must deal with the fact that the Gauss-Poisson covariance matrix depends on the model for the power spectrum of the biased tracers. In the first pass, we treat the standard error on the mean of $\hat{\xi}^{(\ell)}(s)$ across 20 HADES realizations as uncorrelated measurement errors so as to get an estimate of the values of B_1 , B_v , A_{MC} and R_{MC} that best describe the measurements. Of these, the values of B_1 and B_v are then used in a Gauss-Poisson estimate of the measurement covariance for the simulation box, while keeping $A_{\text{MC}} = 0 = R_{\text{MC}}$ for the covariance calculation, to improve the estimate of these parameters using another MCMC run. The resulting best fitting parameter values are then used in a second estimate of the Gauss-Poisson, which is used in a final parameter inference exercise. We find converged results at this point for, both, the best fit values and errors as well as the goodness of fit. The differences between the initial and final estimates of the best fit are also small and statistically insignificant. Below, we report only the results using the full, converged covariance matrix. Our choice of not including MC terms in the covariance estimate is justified *post hoc* by the fact that the MC contribution below is estimated to be small.

In principle, since we know the cosmology for the HADES simulation and because the tracer sample is defined by a simple threshold on halo mass, we can estimate the value of b (the large-scale Eulerian bias of the sample) using a mass-weighted calculation with the

⁵<https://cobaya.readthedocs.io/>

⁶<https://getdist.readthedocs.io/>

⁷<http://class-code.net/>

⁸Recall that the pivot scale is also fixed to $R_p = 2.5h^{-1}\text{Mpc}$; unlike R_* , however, this scale is never varied as a free parameter.

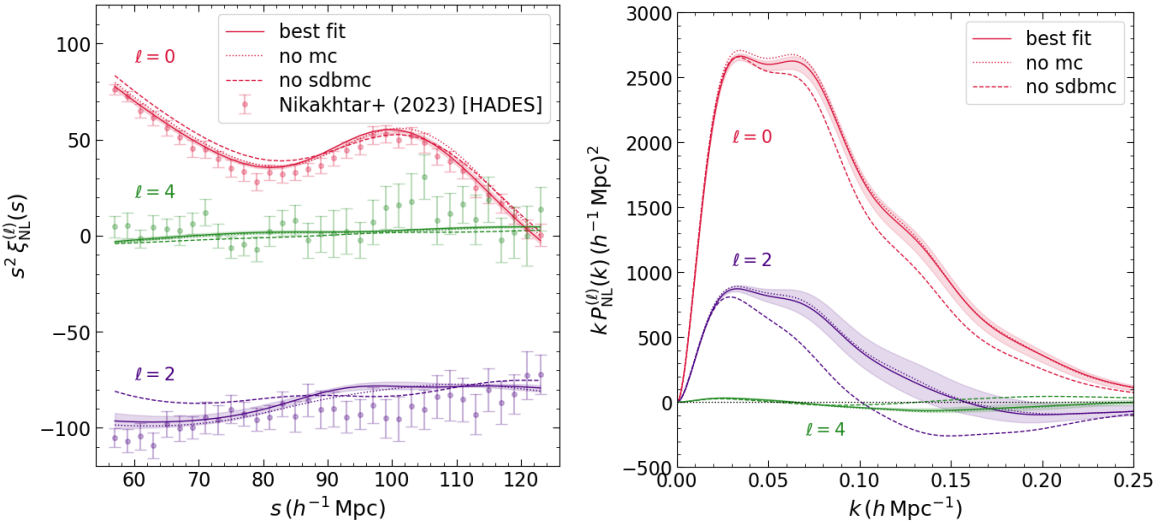


Figure 1. (Left panel): Comparison of the HADES configuration-space measurements from [44] (points with error bars) with the best fitting *sdbmc* model (equation 2.19; solid curves with error bands). For comparison, the dashed curves show the *no sdbmc* model setting the scale-dependent and mode coupling terms to zero, while the dotted curves show the result when setting only the mode coupling terms to zero ($A_{\text{MC}} = 0$) with other parameters set to their best-fit values. (Right panel): Fourier-space results corresponding to the configuration-space ones from the left panel, formatted identically. This analysis used $b = 1.95$ and $R_* = 2.5h^{-1}\text{Mpc}$, with cosmological parameters set to the ones used in the HADES simulations (see text for details).

fitting functions for linear bias and halo mass function from [52] and [53], respectively, which leads to $b = 2.08$. These fitting functions are expected to have a systematic error of about $\sim 5\%$, however. We therefore performed an MCMC analysis varying b along with the 4 *sdbmc* parameters, finding that $b = 1.947^{+0.042}_{-0.031}$ (best fit with central 68% confidence interval) with only weak degeneracies with the other parameters. This is statistically consistent with the expectation from the fitting functions from the literature, when accounting for the $\sim 5\%$ error mentioned above, and is also a more precise estimate ($\lesssim 2\%$ error). In the following, therefore, we fix the large-scale bias to $b = 1.95$.

Fig. 1 shows the best fit model describing the HADES simulation measurements, with Fig. 2 showing the corresponding contour plots of the parameter constraints. The best fitting parameter combination and χ^2 are reported in Table 1. The model is clearly a very good fit. It is also visually clear that the data and the best fitting *sdbmc* model exclude the *no sdbmc* model with substantial statistical significance: the χ^2 value for the *no sdbmc* model is larger than that for the best-fitting *sdbmc* by $\Delta\chi^2 \sim 33$. Also, mode coupling evidently contributes only a small fraction of the total difference between the *sdbmc* and *no sdbmc* results (the dotted curves are very close to the solid ones). This is consistent with theoretical expectations regarding the relative importance of mode coupling effects near the BAO scale for biased tracers (see Appendix B and [29, 33]). The right panels show that these statements are equally valid in Fourier space (see also Appendix A). Importantly, Table 1 and Fig. 2 show that the constraints on the mode coupling smearing scale R_{MC} are in excellent agreement with the theoretical value for σ_v reported in section 3.1 for the HADES simulations.

Interestingly, contrary to the expectation from peaks theory, the measurements prefer a significantly *negative* best-fit value of the velocity bias coefficient B_v . We also see that,

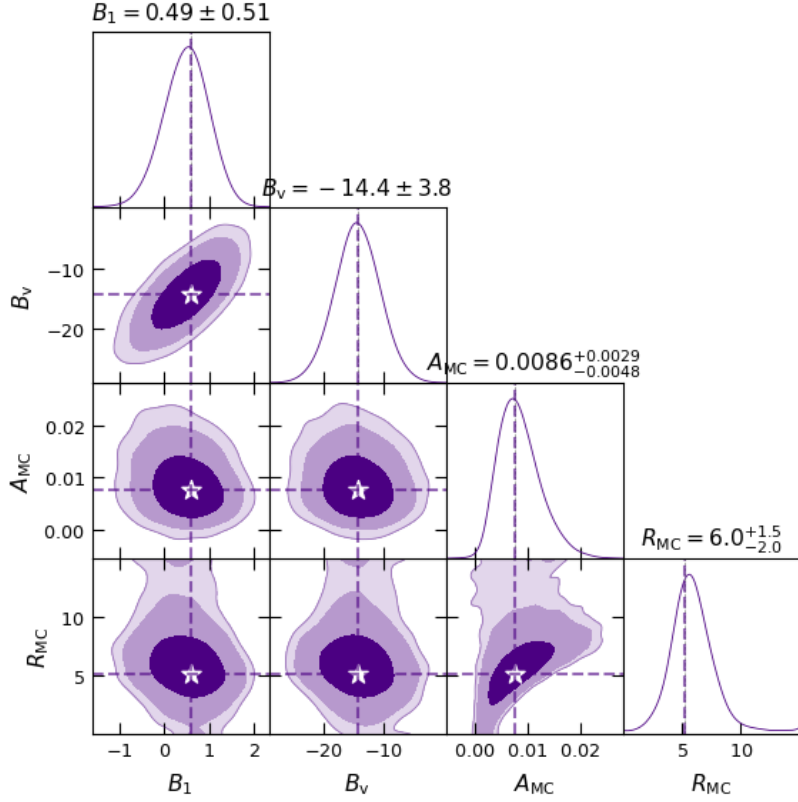


Figure 2. Constraints on *sdbmc* model parameters using the HADES simulation measurements. The contours show the 68%, 95% and 99% confidence regions, and the dashed lines intersecting at the white stars show the best-fit parameter combination. This analysis used $b = 1.95$ and $R_* = 2.5h^{-1}\text{Mpc}$, with cosmological parameters set to the ones used in the HADES simulations (see text for details).

B_1	B_v	A_{MC}	R_{MC} ($h^{-1}\text{Mpc}$)	χ^2/dof	$p\text{-value}$
0.60	-14.3	0.0077	5.2	118.7/98	0.082

Table 1. Best-fit values of the parameters $\{B_1, B_v, A_{\text{MC}}, R_{\text{MC}}\}$ along with the χ^2 per degree of freedom and corresponding p -value from the MCMC analysis of the HADES simulation measurements using the *sdbmc* model. See Fig. 2 for the median and central 68% confidence ranges of each parameter in the respective samples. This analysis used $b = 1.95$ and $R_* = 2.5h^{-1}\text{Mpc}$ (see text for details).

compared to the *no sdbmc* model used by PS23, the best fitting *sdbmc* model predicts a distinctly narrower BAO peak in the monopole $\xi_{\text{NL}}^{(0)}(s)$, which is also shifted to smaller s , and a larger amplitude of variations in the quadrupole $\xi_{\text{NL}}^{(2)}(s)$. The hexadecapole $\xi_{\text{NL}}^{(4)}(s)$, on the other hand, remains featureless, as for the *no sdbmc* case. The analysis in Appendix A shows that these statements continue to hold when fitting the *sdbmc* model to Fourier space measurements at higher redshift. Although the constraints on R_{MC} in this case (Table 2 and Fig. 4) do not agree as well with the expected value σ_v in the MINERVA simulations, this is perhaps not surprising, given the limited range of validity of our approximation in Fourier space.

These results together underline the need for modelling the effects of scale-dependent bias at BAO scales, without which the inference of cosmological parameters could be substantially biased. E.g., since the *no sdbmc* model has a broader BAO feature than the best fitting *sdbmc* one, ignoring scale-dependent bias but allowing the large-scale bias b to be free would at least lead to a significantly lower value of b (driven by the data at $s \lesssim 80h^{-1}\text{Mpc}$ and $s \gtrsim 110h^{-1}\text{Mpc}$), in addition to a degradation of the quality of the fit (due to not being able to match the width of the BAO feature), in Fig. 1. This would in turn potentially bias any constraints on parameters such as f or σ_8 which have well-known degeneracies with b .

4.2 Model variations

Our models for the scale dependence of bias and mode coupling, although well-motivated as discussed in section 2.2 and Appendix B, are nevertheless somewhat *ad hoc*. To assess the impact of various choices in the model setup and our analysis above, we also explored some variations which we briefly report below.

4.2.1 Scale-dependent bias

First, we considered the impact of allowing the smoothing scale R_* to be free in the configuration space analysis, leading to 5 free parameters in the model. In this case, the value of R_* is only weakly constrained with a best fit close to $\sim 5h^{-1}\text{Mpc}$, but still fully consistent with $2.5h^{-1}\text{Mpc}$, and shows a strong degeneracy with B_1 . The values of the other parameters are consistent with those reported in Table 1 and Fig. 2, but with larger errors. In other words, the BAO-scale 2pcf measurements with DESI-like surveys are only weakly sensitive to the shape/scale of the smoothing filter defining scale-dependent bias.

This has some consequences for our eventual goal of model-agnostic inference. The structure of equations (2.16) and (2.22) shows that R_* only appears in the combination $e^{-k^2(\sigma_v^2 + R_*^2)}$. In a model-agnostic inference exercise, σ_v would be treated as a free parameter. Despite the fact that σ_v also appears in other factors such as $e^{-K^2\mu_k^2}$ in equation (2.22), its appearance along with R_*^2 implies that these parameters will likely be highly degenerate in a model-agnostic setting. This will need to be accounted for in any exercise aimed at constraining cosmological parameters like σ_v ; we will discuss this further in future work.

Next, we also explored a more complex model of scale dependence, still within the Laplace-Gauss expansion framework, in which we allowed separate Gaussian smearing scales for the density and velocity bias factors, combined in a structure motivated by the shapes of the curves seen in fig. 1 of [38]. However, the resulting 4-parameter model showed strong degeneracies in the parameters, without improving the quality of description of the clustering measurements. We conclude that our 3-parameter description of scale-dependent bias in equations (2.14) and (2.15) is sufficiently accurate and simple for our purposes.

4.2.2 Mode coupling

While the scale-dependence of density and velocity bias has been discussed widely in the literature, the effects of mode coupling for biased tracers have attracted considerably less attention. In part, this may be because, in Fourier space, the leading order effects of mode coupling are degenerate with those of scale dependent bias and are consequently treated as being part of ‘counter terms’ in effective field theory (EFT) treatments [54].

Although our model separates out the effects of mode coupling, we recall that the discussion in Appendix B and our implementation in (2.17) (equivalently, equations 2.21 and 2.23) implies that the mode coupling term depends on the scale-dependent bias of the

tracers. To assess the impact of this feature of the model, we repeated our analysis by replacing the occurrence of $B(k, \mu_k)$ in equation (2.23) with $1 + \beta \mu_k^2$. We found only statistically insignificant differences in the resulting parameter constraints and quality of fit. This indicates that, in practical terms, the constraints on the mode coupling piece are relatively insensitive to the details of scale-dependent bias. Together with the fact, noted earlier, that the mode coupling contribution is relatively small, this reassures us that our specific implementation of mode coupling is unlikely to produce biases in parameter recovery. We do advocate retaining the mode coupling contribution, given that its amplitude is constrained to be positive at $> 95\%$ confidence (c.f. Fig. 2).

5 Conclusion

Exploiting the BAO feature for model-agnostic cosmological inference is a challenging current problem for upcoming surveys such as DESI and Euclid. As identified by PS23, one bottleneck in these efforts is the modelling of the scale dependence of galaxy bias, along with the effects of mode coupling, both of which are nonlinear effects that are known to modify the shape and location of the BAO feature. Modelling these effects in redshift space is critical in order to build robust model-agnostic frameworks for cosmological inference.

In this work, using simple and well-motivated models for the scale dependence of Lagrangian density and velocity bias and the effects of mode coupling, we have shown how to model the redshift-space multipoles of the 2-point correlation function (2pcf) accounting for these effects. Our model draws inspiration from the application of the Zel'dovich approximation to peaks theory (e.g., section 2.2 and Appendix B) and is agnostic to the details of the cosmological model, in that the predictions for the multipoles can be calculated for arbitrary linear power spectra. We have validated the model using Λ CDM simulations, finding that it can accurately describe the 2pcf multipoles $\xi_{\text{NL}}^{(\ell)}(s)$ for $55 \lesssim s/(h^{-1}\text{Mpc}) \lesssim 125$, i.e., near the BAO feature, for realistic tracer samples in configuration space. (In Appendix A, we also show that the model works well in Fourier space for $k \lesssim 0.13h \text{ Mpc}^{-1}$, although this is less relevant for the model-agnostic applications we have in mind.)

Our model in equation (2.17) introduced a total of 5 new parameters: three of these $\{B_1, B_v, R_*\}$ describe the effects of scale-dependent bias, while the other two $\{A_{\text{MC}}, R_{\text{MC}}\}$ additionally model the contribution of mode coupling. While this model allowed for the mode coupling contribution to be smeared by a scale R_{MC} that is not necessarily equal to the expected theoretical value of σ_v , our analysis of the HADES simulation in fact showed that it is perfectly acceptable to set $R_{\text{MC}} = \sigma_v$. This would lead to a very useful reduction of the parameter space in future work, where σ_v will be varied as a free parameter.

A key advantage of our model is that it falls within the class of ‘Laplace-Gauss’ expansions which were discussed by PS23 as being particularly useful in model-agnostic inference using the BAO feature in redshift space. A Laplace-Gauss expansion in Fourier space, i.e., an expression involving powers of k^2 multiplying terms like $e^{-k^2\sigma^2}$, combines naturally with the Zel'dovich smearing represented by the term $e^{-k^2\sigma_v^2}$ in the ‘propagator’ term in equation (2.22). In forthcoming work, we will show how this can be leveraged to build Zel'dovich smearing approximations that account for both scale-dependent bias as well as mode coupling. Together with a set of well-motivated minimal basis functions for describing the linear theory 2pcf of real space matter fluctuations $\xi_{\text{lin}}(r)$ [e.g., 22, 55, 56], this will help develop a complete framework for model-agnostic inference of cosmological parameters such as f , σ_v and the BAO scale.

Acknowledgments

We are grateful to F. Nikakhtar for providing the multipole measurements in the HADES simulations. The research of AP is supported by the Associates Scheme of ICTP, Trieste. AP and RKS thank ICTP, Trieste for hospitality during the summer of 2024 when part of this work was completed. This work made extensive use of the open source computing packages NumPy [57]⁹, SciPy [58]¹⁰, Matplotlib [59]¹¹ and Jupyter Notebook.¹²

References

- [1] D.J. Eisenstein, I. Zehavi, D.W. Hogg, R. Scoccimarro, M.R. Blanton, R.C. Nichol et al., *Detection of the Baryon Acoustic Peak in the Large-Scale Correlation Function of SDSS Luminous Red Galaxies*, *ApJ* **633** (2005) 560 [[astro-ph/0501171](https://arxiv.org/abs/astro-ph/0501171)].
- [2] S. Cole, W.J. Percival, J.A. Peacock, P. Norberg, C.M. Baugh, C.S. Frenk et al., *The 2dF Galaxy Redshift Survey: power-spectrum analysis of the final data set and cosmological implications*, *MNRAS* **362** (2005) 505 [[astro-ph/0501174](https://arxiv.org/abs/astro-ph/0501174)].
- [3] L. Anderson, E. Aubourg, S. Bailey, D. Bizyaev, M. Blanton, A.S. Bolton et al., *The clustering of galaxies in the SDSS-III Baryon Oscillation Spectroscopic Survey: baryon acoustic oscillations in the Data Release 9 spectroscopic galaxy sample*, *MNRAS* **427** (2012) 3435 [[1203.6594](https://arxiv.org/abs/1203.6594)].
- [4] L. Anderson, E. Aubourg, S. Bailey, F. Beutler, A.S. Bolton, J. Brinkmann et al., *The clustering of galaxies in the SDSS-III Baryon Oscillation Spectroscopic Survey: measuring D_A and H at $z = 0.57$ from the baryon acoustic peak in the Data Release 9 spectroscopic Galaxy sample*, *MNRAS* **439** (2014) 83 [[1303.4666](https://arxiv.org/abs/1303.4666)].
- [5] S. Alam, M. Ata, S. Bailey, F. Beutler, D. Bizyaev, J.A. Blazek et al., *The clustering of galaxies in the completed SDSS-III Baryon Oscillation Spectroscopic Survey: cosmological analysis of the DR12 galaxy sample*, *MNRAS* **470** (2017) 2617 [[1607.03155](https://arxiv.org/abs/1607.03155)].
- [6] S. Bottaro, E. Castorina, M. Costa, D. Redigolo and E. Salvioni, *Unveiling Dark Forces with Measurements of the Large Scale Structure of the Universe*, *Phys. Rev. Lett.* **132** (2024) 201002 [[2309.11496](https://arxiv.org/abs/2309.11496)].
- [7] R. Mauland, H.A. Winther and C.-Z. Ruan, *Sesame: A power spectrum emulator pipeline for beyond- Λ CDM models*, *a_(p)* **685** (2024) A156 [[2309.13295](https://arxiv.org/abs/2309.13295)].
- [8] S. Paradiso, G. McGee and W.J. Percival, *Evaluating extensions to Λ CDM: an application of Bayesian model averaging and selection*, *arXiv e-prints* (2024) arXiv:2403.02120 [[2403.02120](https://arxiv.org/abs/2403.02120)].
- [9] A.J. Cuesta, M. Vargas-Magaña, F. Beutler, A.S. Bolton, J.R. Brownstein, D.J. Eisenstein et al., *The clustering of galaxies in the SDSS-III Baryon Oscillation Spectroscopic Survey: baryon acoustic oscillations in the correlation function of LOWZ and CMASS galaxies in Data Release 12*, *MNRAS* **457** (2016) 1770 [[1509.06371](https://arxiv.org/abs/1509.06371)].
- [10] F. Beutler, H.-J. Seo, S. Saito, C.-H. Chuang, A.J. Cuesta, D.J. Eisenstein et al., *The clustering of galaxies in the completed SDSS-III Baryon Oscillation Spectroscopic Survey: anisotropic galaxy clustering in Fourier space*, *MNRAS* **466** (2017) 2242 [[1607.03150](https://arxiv.org/abs/1607.03150)].
- [11] M. Blomqvist, H. du Mas des Bourboux, N.G. Busca, V. de Sainte Agathe, J. Rich, C. Balland et al., *Baryon acoustic oscillations from the cross-correlation of Ly α absorption and quasars in eBOSS DR14*, *a_(p)* **629** (2019) A86 [[1904.03430](https://arxiv.org/abs/1904.03430)].

⁹<http://www.numpy.org>

¹⁰<http://www.scipy.org>

¹¹<https://matplotlib.org/>

¹²<https://jupyter.org>

[12] H. du Mas des Bourboux, J. Rich, A. Font-Ribera, V. de Sainte Agathe, J. Farr, T. Etourneau et al., *The Completed SDSS-IV Extended Baryon Oscillation Spectroscopic Survey: Baryon Acoustic Oscillations with Ly α Forests*, *ApJ* **901** (2020) 153 [[2007.08995](#)].

[13] H. Gil-Marín, J.E. Bautista, R. Paviot, M. Vargas-Magaña, S. de la Torre, S. Fromenteau et al., *The Completed SDSS-IV extended Baryon Oscillation Spectroscopic Survey: measurement of the BAO and growth rate of structure of the luminous red galaxy sample from the anisotropic power spectrum between redshifts 0.6 and 1.0*, *MNRAS* **498** (2020) 2492 [[2007.08994](#)].

[14] E. Noda, M. Peloso and M. Pietroni, *Extracting the BAO scale from BOSS DR12 dataset*, *Physics of the Dark Universe* **29** (2020) 100579 [[1901.06854](#)].

[15] T.M.C. Abbott, M. Aguena, S. Allam, A. Amon, F. Andrade-Oliveira, J. Asorey et al., *Dark Energy Survey Year 3 results: A 2.7% measurement of baryon acoustic oscillation distance scale at redshift 0.835*, *Phys. Rev. D* **105** (2022) 043512 [[2107.04646](#)].

[16] I. Babić, F. Schmidt and B. Tucci, *Straightening the Ruler: Field-Level Inference of the BAO Scale with LEFTfield*, *arXiv e-prints* (2024) [arXiv:2407.01524](#) [[2407.01524](#)].

[17] I. Babić, F. Schmidt and B. Tucci, *Forward vs Backward: Improving BAO Constraints with Field-Level Inference*, *arXiv e-prints* (2025) [arXiv:2505.13588](#) [[2505.13588](#)].

[18] S. Anselmi, G.D. Starkman and R.K. Sheth, *Beating non-linearities: improving the baryon acoustic oscillations with the linear point*, *MNRAS* **455** (2016) 2474 [[1508.01170](#)].

[19] S. Anselmi, P.-S. Corasaniti, G.D. Starkman, R.K. Sheth and I. Zehavi, *Linear point standard ruler for galaxy survey data: Validation with mock catalogs*, *Phys. Rev. D* **98** (2018) 023527 [[1711.09063](#)].

[20] S. Anselmi, G.D. Starkman, P.-S. Corasaniti, R.K. Sheth and I. Zehavi, *Galaxy Correlation Functions Provide a More Robust Cosmological Standard Ruler*, *Phys. Rev. Lett.* **121** (2018) 021302 [[1703.01275](#)].

[21] F. Nikakhtar, R.K. Sheth and I. Zehavi, *Laguerre reconstruction of the correlation function on baryon acoustic oscillation scales*, *Phys. Rev. D* **104** (2021) 043530 [[2101.08376](#)].

[22] F. Nikakhtar, R.K. Sheth and I. Zehavi, *Laguerre reconstruction of the BAO feature in halo-based mock galaxy catalogues*, *Phys. Rev. D* **104** (2021) 063504 [[2107.12537](#)].

[23] A. Paranjape and R.K. Sheth, *Bayesian evidence comparison for distance scale estimates*, *MNRAS* **517** (2022) 4696 [[2209.00668](#)].

[24] A. Paranjape and R.K. Sheth, *Model-agnostic cosmological constraints from the baryon acoustic oscillation feature in redshift space*, *MNRAS* (2023) [[2304.09198](#)].

[25] S. Bharadwaj, *The Evolution of Correlation Functions in the Zeldovich Approximation and Its Implications for the Validity of Perturbation Theory*, *ApJ* **472** (1996) 1 [[astro-ph/9606121](#)].

[26] M. Crocce and R. Scoccimarro, *Memory of initial conditions in gravitational clustering*, *Phys. Rev. D* **73** (2006) 063520 [[astro-ph/0509419](#)].

[27] DESI Collaboration, A. Aghamousa, J. Aguilar, S. Ahlen, S. Alam, L.E. Allen et al., *The DESI Experiment Part I: Science, Targeting, and Survey Design*, *arXiv e-prints* (2016) [arXiv:1611.00036](#) [[1611.00036](#)].

[28] DESI Collaboration, A.G. Adame, J. Aguilar, S. Ahlen, S. Alam, D.M. Alexander et al., *DESI 2024 VI: Cosmological Constraints from the Measurements of Baryon Acoustic Oscillations*, *arXiv e-prints* (2024) [arXiv:2404.03002](#) [[2404.03002](#)].

[29] V. Desjacques, M. Crocce, R. Scoccimarro and R.K. Sheth, *Modeling scale-dependent bias on the baryonic acoustic scale with the statistics of peaks of Gaussian random fields*, *Phys. Rev. D* **82** (2010) 103529 [[1009.3449](#)].

[30] S. Gaines, F. Nikakhtar, N. Padmanabhan and R.K. Sheth, *Leveraging protohalos and scale-dependent bias to calibrate the BAO scale in real space*, *Phys. Rev. D* **110** (2024) 103511 [[2408.00072](#)].

[31] M. Marinucci, K. Pardede and M. Pietroni, *Bootstrapping Lagrangian Perturbation Theory for the Large Scale Structure*, *arXiv e-prints* (2024) arXiv:2405.08413 [[2405.08413](#)].

[32] M. Crocce and R. Scoccimarro, *Renormalized cosmological perturbation theory*, *Phys. Rev. D* **73** (2006) 063519 [[astro-ph/0509418](#)].

[33] M. Crocce and R. Scoccimarro, *Nonlinear evolution of baryon acoustic oscillations*, *Phys. Rev. D* **77** (2008) 023533 [[0704.2783](#)].

[34] A.N. Taylor and A.J.S. Hamilton, *Non-linear cosmological power spectra in real and redshift space*, *MNRAS* **282** (1996) 767 [[astro-ph/9604020](#)].

[35] V. Desjacques and R.K. Sheth, *Redshift space correlations and scale-dependent stochastic biasing of density peaks*, *Phys. Rev. D* **81** (2010) 023526 [[0909.4544](#)].

[36] M. Peloso, M. Pietroni, M. Viel and F. Villaescusa-Navarro, *The effect of massive neutrinos on the BAO peak*, *J. Cosmology Astropart. Phys.* **2015** (2015) 001 [[1505.07477](#)].

[37] N. Kaiser, *Clustering in real space and in redshift space*, *MNRAS* **227** (1987) 1.

[38] T. Baldauf, V. Desjacques and U. Seljak, *Velocity bias in the distribution of dark matter halos*, *Phys. Rev. D* **92** (2015) 123507 [[1405.5885](#)].

[39] A. Paranjape, O. Hahn and R.K. Sheth, *Halo assembly bias and the tidal anisotropy of the local halo environment*, *MNRAS* **476** (2018) 3631 [[1706.09906](#)].

[40] R.K. Sheth, H.J. Mo and G. Tormen, *Ellipsoidal collapse and an improved model for the number and spatial distribution of dark matter haloes*, *MNRAS* **323** (2001) 1 [[arXiv:astro-ph/9907024](#)].

[41] R.K. Sheth and G. Tormen, *An excursion set model of hierarchical clustering: ellipsoidal collapse and the moving barrier*, *MNRAS* **329** (2002) 61 [[astro-ph/0105113](#)].

[42] E. Castorina, A. Paranjape, O. Hahn and R.K. Sheth, *Excursion set peaks: the role of shear*, *arXiv e-prints* (2016) [[1611.03619](#)].

[43] F. Villaescusa-Navarro, A. Banerjee, N. Dalal, E. Castorina, R. Scoccimarro, R. Angulo et al., *The Imprint of Neutrinos on Clustering in Redshift Space*, *ApJ* **861** (2018) 53 [[1708.01154](#)].

[44] F. Nikakhtar, N. Padmanabhan, B. Lévy, R.K. Sheth and R. Mohayaee, *Optimal transport reconstruction of biased tracers in redshift space*, *Phys. Rev. D* **108** (2023) 083534 [[2307.03671](#)].

[45] J.N. Grieb, A.G. Sánchez, S. Salazar-Albornoz and C. Dalla Vecchia, *Gaussian covariance matrices for anisotropic galaxy clustering measurements*, *MNRAS* **457** (2016) 1577 [[1509.04293](#)].

[46] S. Alam, F.D. Albareti, C. Allende Prieto, F. Anders, S.F. Anderson, T. Anderton et al., *The Eleventh and Twelfth Data Releases of the Sloan Digital Sky Survey: Final Data from SDSS-III*, *ApJS* **219** (2015) 12 [[1501.00963](#)].

[47] J. Torrado and A. Lewis, “Cobaya: Bayesian analysis in cosmology.” *Astrophysics Source Code Library*, record ascl:1910.019, Oct., 2019.

[48] J. Torrado and A. Lewis, *Cobaya: code for Bayesian analysis of hierarchical physical models*, *J. Cosmology Astropart. Phys.* **2021** (2021) 057 [[2005.05290](#)].

[49] A. Lewis, *GetDist: a Python package for analysing Monte Carlo samples*, *arXiv e-prints* (2019) arXiv:1910.13970 [[1910.13970](#)].

[50] J. Lesgourgues, *The Cosmic Linear Anisotropy Solving System (CLASS) I: Overview*, *arXiv e-prints* (2011) arXiv:1104.2932 [[1104.2932](#)].

- [51] D. Blas, J. Lesgourgues and T. Tram, *The Cosmic Linear Anisotropy Solving System (CLASS). Part II: Approximation schemes*, *J. Cosmology Astropart. Phys.* **2011** (2011) 034 [[1104.2933](#)].
- [52] J.L. Tinker, B.E. Robertson, A.V. Kravtsov, A. Klypin, M.S. Warren, G. Yepes et al., *The Large-scale Bias of Dark Matter Halos: Numerical Calibration and Model Tests*, *ApJ* **724** (2010) 878 [[1001.3162](#)].
- [53] J. Tinker, A.V. Kravtsov, A. Klypin, K. Abazajian, M. Warren, G. Yepes et al., *Toward a Halo Mass Function for Precision Cosmology: The Limits of Universality*, *ApJ* **688** (2008) 709 [[0803.2706](#)].
- [54] J.J.M. Carrasco, M.P. Hertzberg and L. Senatore, *The effective field theory of cosmological large scale structures*, *Journal of High Energy Physics* **2012** (2012) 82 [[1206.2926](#)].
- [55] J.J. Lee, F. Nikakhtar, A. Paranjape and R.K. Sheth, *Eigen-decomposition of Covariance matrices: An application to the BAO Linear Point*, *arXiv e-prints* (2024) arXiv:2407.04692 [[2407.04692](#)].
- [56] A. Paranjape and R.K. Sheth, *Model-agnostic basis functions for the 2-point correlation function of dark matter in linear theory*, *arXiv e-prints* (2024) arXiv:2410.21374 [[2410.21374](#)].
- [57] S. Van Der Walt, S.C. Colbert and G. Varoquaux, *The NumPy array: a structure for efficient numerical computation*, *ArXiv e-prints* (2011) [[1102.1523](#)].
- [58] P. Virtanen, R. Gommers, T.E. Oliphant, M. Haberland, T. Reddy, D. Cournapeau et al., *SciPy 1.0: Fundamental Algorithms for Scientific Computing in Python*, *Nature Methods* **17** (2020) 261.
- [59] J.D. Hunter, *Matplotlib: A 2d graphics environment*, *Computing In Science & Engineering* **9** (2007) 90.
- [60] T. Baldauf and V. Desjacques, *Phenomenology of baryon acoustic oscillation evolution from Lagrangian to Eulerian space*, *Phys. Rev. D* **95** (2017) 043535 [[1612.04521](#)].
- [61] T. Matsubara, *Velocity bias and the nonlinear perturbation theory of peaks*, *Phys. Rev. D* **100** (2019) 083504 [[1907.13251](#)].
- [62] V. Desjacques and R.K. Sheth, *Redshift space correlations and scale-dependent stochastic biasing of density peaks*, *Phys. Rev. D* **81** (2010) 023526 [[0909.4544](#)].

A Fourier space results

Here, we test whether the *sdbmc* model described in the main text can also describe redshift space non-linearities in Fourier space, by comparing the Fourier space counterparts $\Delta_{\text{NL}}^{(\ell)2}(k)$ of the multipoles $\xi_{\text{NL}}^{(\ell)}(s)$ with corresponding measurements at $z = 0.57$ in the simulations of [45].

While $\Delta_{\text{prop}}^{(\ell)2}(k)$ in equation (2.22) can be identified as the Fourier space multipole of the ‘propagator’ term, the structure of equation (2.21) shows that $\Delta_{\text{L}}^{(\ell)2}(k)$ in equation (2.23) is not equal to the Fourier multipole $\Delta_{\text{MC}}^{(\ell)2}(k)$ of the mode coupling term, rather, it is the multipole of the linear theory anisotropic power spectrum (modified by the scale-dependent bias terms). Instead, we have

$$\Delta_{\text{MC}}^{(\ell)2}(k) = \frac{2k^3}{\pi} (-i)^\ell \int_0^\infty ds s^2 j_\ell(ks) \xi_{\text{MC}}^{(\ell)}(s) \quad (\text{A.1})$$

To simplify this, we define the integral $\mathcal{I}_\ell(k, k')$ as

$$\mathcal{I}_\ell(k, k') \equiv \int_0^\infty ds s^3 j_\ell(ks) j_{\ell+1}(k's), \quad (\text{A.2})$$

which leads to

$$\begin{aligned} \Delta_{\text{MC}}^{(\ell)2}(k) &= \frac{2k^3}{\pi} (-i)^\ell \int_0^\infty ds s^2 j_\ell(ks) \xi_{\text{MC}}^{(\ell)}(s) \\ &= A_{\text{MC}} \frac{2k^3}{\pi} (-i^2)^\ell \int d \ln k' \Delta_{\text{L}}^{(\ell)2}(k') \int_0^\infty ds s^2 j_\ell(ks) [\ell j_\ell(k's) - k's j_{\ell+1}(k's)] \\ &= A_{\text{MC}} \frac{2k^3}{\pi} \int_0^\infty dk' \Delta_{\text{L}}^{(\ell)2}(k') \left[\frac{\ell \pi}{2k^3} \delta_{\text{D}}(k - k') - \mathcal{I}_\ell(k, k') \right] \\ &= A_{\text{MC}} \left[\ell \Delta_{\text{L}}^{(\ell)2}(k) - \frac{2k^3}{\pi} \int_0^\infty dk' \Delta_{\text{L}}^{(\ell)2}(k') \mathcal{I}_\ell(k, k') \right], \end{aligned} \quad (\text{A.3})$$

where we used the closure identity

$$\int_0^\infty dx x^2 j_\ell(ax) j_\ell(bx) = \frac{\pi}{2a^2} \delta_{\text{D}}(a - b). \quad (\text{A.4})$$

To proceed further, we use the recursion relation

$$j_{\ell+1}(x) = (2\ell + 1) j_\ell(x)/x - j_{\ell-1}(x), \quad (\text{A.5})$$

along with the closure relation (A.4) to derive the recursion relation

$$\mathcal{I}_{\ell+1}(k, k') = \frac{(2\ell + 1)\pi}{2k^3} \delta_{\text{D}}(k - k') - \mathcal{I}_{\ell-1}(k', k). \quad (\text{A.6})$$

Note the exchange of arguments in the last term. This recursion can be used if we have an explicit expression for $\mathcal{I}_0(k, k')$, which can be derived as follows.

$$\begin{aligned} \mathcal{I}_0(k, k') &= \int_0^\infty ds s^3 \frac{\sin(ks)}{ks} \frac{1}{k'^2 s^2} [\sin(k's) - k's \cos(k's)] \\ &= \int_0^\infty ds \frac{\sin(ks)}{kk'^2} [\sin(k's) - k's \cos(k's)] \\ \therefore \mathcal{I}_0(k, k') &= \frac{\pi}{2kk'} \left[\frac{1}{k'} (\delta_{\text{D}}(k - k') - \delta_{\text{D}}(k + k')) - \frac{\partial}{\partial k'} (\delta_{\text{D}}(k - k') - \delta_{\text{D}}(k + k')) \right], \end{aligned} \quad (\text{A.7})$$

where we used the Dirac delta expression $\int_{-\infty}^\infty dx e^{iak} = 2\pi \delta_{\text{D}}(a)$ to write

$$\int_0^\infty dx \sin(ax) \sin(bx) = \frac{\pi}{2} [\delta_{\text{D}}(a - b) - \delta_{\text{D}}(a + b)], \quad (\text{A.8})$$

$$\int_0^\infty dx x \sin(ax) \cos(bx) = \frac{\pi}{2} \frac{\partial}{\partial b} [\delta_{\text{D}}(a - b) - \delta_{\text{D}}(a + b)]. \quad (\text{A.9})$$

We also note that the terms involving $\delta_{\text{D}}(k + k')$ in equation (A.7) will never contribute, since $k > 0$ and the integral over k' is also always restricted to positive values in equation (A.3), so that we have

$$\frac{2k^3}{\pi} \int_0^\infty dk' F(k') \mathcal{I}_0(k, k') = k \partial_k F, \quad (\text{A.10})$$

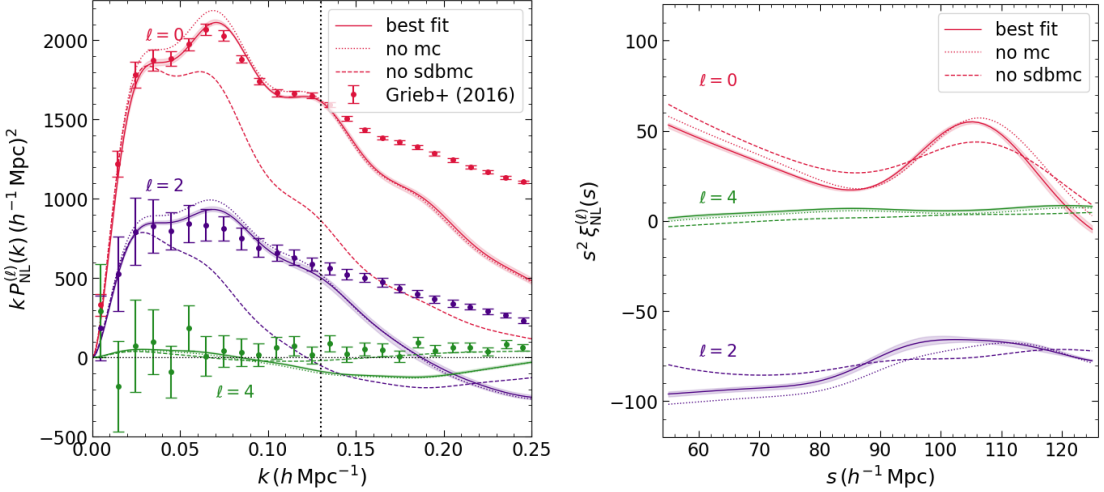


Figure 3. (Left panel): Comparison of the Fourier-space measurements from [45] (points with error bars) with the best fitting *sdbmc* model (equation A.14; solid curves with error bands). For comparison, the dashed curves show the *no sdbmc* model (equation 2.6) and the dotted curves show the result of setting $A_{\text{MC}} = 0$ in the best-fit *sdbmc* model (c.f. Fig. 1). Vertical dotted line indicates the threshold $k_{\text{max}} = 0.13 h \text{ Mpc}^{-1}$; the likelihood was evaluated using data with $k < k_{\text{max}}$. (Right panel): Configuration space results corresponding the the Fourier-space ones from the left panel, formatted identically. This analysis used $b = 2.005$ and $R_* = 2.5 h^{-1} \text{ Mpc}$, with cosmological parameters set to the ones used by [45] (see text for details).

for any function $F(k)$.

A straightforward calculation using equations (A.6) and (A.7) in equation (A.3) now gives

$$\Delta_{\text{MC}}^{(0)2}(k) = -A_{\text{MC}} k \partial_k \Delta_{\text{L}}^{(0)2}(k), \quad (\text{A.11})$$

$$\Delta_{\text{MC}}^{(2)2}(k) = -A_{\text{MC}} k \partial_k \Delta_{\text{L}}^{(2)2}(k), \quad (\text{A.12})$$

$$\Delta_{\text{MC}}^{(4)2}(k) = A_{\text{MC}} \left(4\Delta_{\text{L}}^{(4)2}(k) + k \partial_k \Delta_{\text{L}}^{(4)2}(k) \right). \quad (\text{A.13})$$

These expressions are useful in comparing this model to the k -space multipole measurements of [45]. The *sdbmc* model including effects of scale-dependent bias and mode coupling is then

$$\Delta_{\text{NL}}^{(\ell)2}(k) = \Delta_{\text{prop}}^{(\ell)2}(k) + \Delta_{\text{MC}}^{(\ell)2}(k), \quad (\text{A.14})$$

with $\Delta_{\text{prop}}^{(\ell)2}(k)$ given by equation (2.22) and $\Delta_{\text{MC}}^{(\ell)2}(k)$ by equations (A.11)-(A.13).

The results of varying the 4 parameters $\{B_1, B_v, A_{\text{MC}}, R_{\text{MC}}\}$ using the MCMC technique with broad uniform priors is shown in Figs. 3 and 4. Since we expect the *sdbmc* model to break down at small scales, we restrict the data used in the likelihood calculation to wave numbers smaller than k_{max} , whose value we discuss below.

From the *left panel* of Fig. 3 and Table 2, we see that, similarly to the configuration space results in the main text, the *sdbmc* model is capable of producing an excellent description of the simulation measurements at $k < k_{\text{max}}$. The *right panel* of Fig. 3 shows the corresponding predictions in configuration space near the BAO feature. Fig. 4 shows that this fit is achieved by a parameter combination in which *all* 4 parameters are significantly non-zero, with values

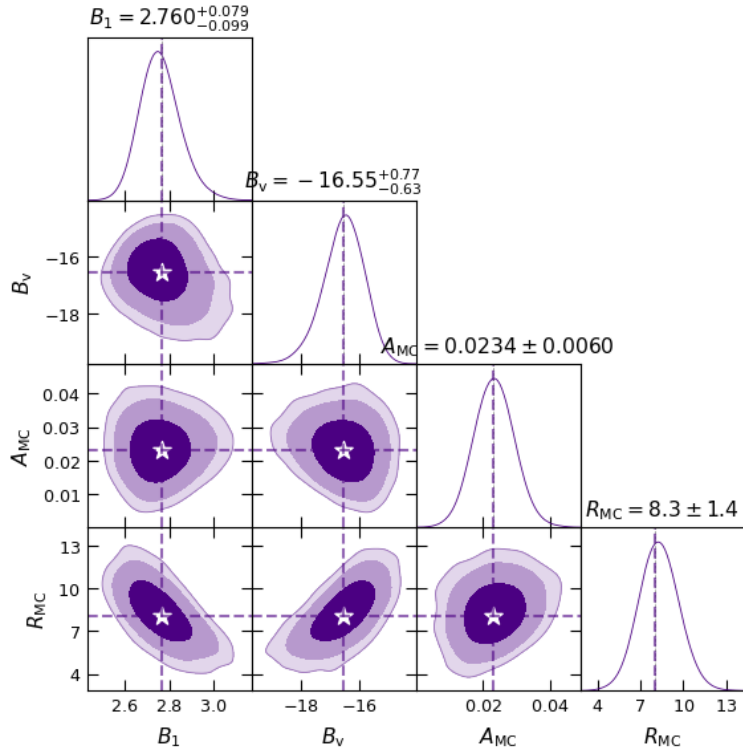


Figure 4. Constraints on *sdbmc* model parameters using the Fourier space measurements of [45]. The contours show the 68%, 95% and 99% confidence regions, and the dashed lines intersecting at the white stars show the best-fit parameter combination. This analysis used $b = 2.005$ and $R_* = 2.5h^{-1}\text{Mpc}$, with cosmological parameters set to the ones used by [45] (see text for details).

B_1	B_v	A_{MC}	R_{MC} ($h^{-1}\text{Mpc}$)	χ^2/dof	$p\text{-value}$
2.764	-16.55	0.0230	8.1	41.55/35	0.25

Table 2. Best-fit values of the parameters $\{B_1, B_v, A_{\text{MC}}, R_{\text{MC}}\}$ along with the χ^2 per degree of freedom and corresponding p -value from the MCMC analysis of the Fourier space measurements of [45] using the *sdbmc* model. See Fig. 4 for the median and central 68% confidence ranges of each parameter in the respective samples.

that are broadly similar to those seen for the $z = 0$ configuration space results in the main text. The parameter values can, in principle, depend not only on the tracer selection and epoch of observation but also on the cosmology which is slightly different between the two simulations. The differences between the best fitting *sdbmc* and the *no sdbmc* models are also similar to those discussed in the main text, with the difference between the monopoles being more pronounced.

The results in Figs. 3 and 4 used $k_{\text{max}} = 0.13 h \text{Mpc}^{-1}$. We have checked that increasing k_{max} substantially degrades the goodness-of-fit with steadily changing best fit parameter values, while decreasing it gives a comparable goodness-of-fit and stable best fit parameter values but with wider parameter constraints. This suggests that $k < k_{\text{max}} = 0.13 h \text{Mpc}^{-1}$ is a good indicator of the validity of the *sdbmc* model as applied to the measurements from [45].

It is possible that the value of k_{\max} depends on the choice of halo configuration, cosmology, etc., but it suffices for our purposes to note that the *sdbmc* model is an accurate description of anisotropic clustering at *substantially* smaller scales than the model without scale-dependent bias and mode coupling (dashed lines in Fig. 3).

B Accuracy and generality of our treatment of mode coupling

In the main text, we noted that the real space model is ‘smeared’, biased linear theory plus a mode-coupling piece, and the redshift space model has a μ -dependent ‘Kaiser’ pre-factor times μ -dependent smearing. However, without further comment, this is ambiguous, in that it does not specify if the ‘bias’ factors are ‘Lagrangian’ or ‘Eulerian’, nor how the Kaiser factor arises. In Lagrangian bias models, there is no ambiguity: as time goes on, the smearing increases, the bias evolves from Lagrangian to Eulerian, and the Kaiser factor is also generated, all self-consistently. In particular, in the Zeldovich approximation, the redshift-space coordinate \mathbf{x}_s at late times is related to the initial coordinate \mathbf{q} by

$$\mathbf{x}_s = \mathbf{q} + \mathbf{S}(\mathbf{q}) + f\mathbf{S}(\mathbf{q}) \cdot \hat{\mathbf{z}} \quad (\text{B.1})$$

where $\mathbf{S}(\mathbf{q})$ is the gradient of the gravitational potential $\phi(\mathbf{q})$. As a result, the redshift-space distorted power spectrum is [29, 60, 61]

$$\frac{P_{\text{Zel}}^s(k, \mu)}{G(k, \mu)} \approx \left[b_1^L(k) + b_{\text{vel}}(k)(1 + f\mu^2) \right]^2 P_L(k) + P_{\text{1loop}}^s(k, \mu), \quad (\text{B.2})$$

where μ is the cosine of the angle between vector \mathbf{k} and the line-of-sight, and

$$\begin{aligned} P_{\text{1loop}}^s(k, \mu) = & \int d\mathbf{k}_1 P_L(k_1) \int d\mathbf{k}_2 P_L(k_2) \left[b_2^L(\mathbf{k}_1, \mathbf{k}_2) + b_{\text{vel}}(\mathbf{k}_1)b_{\text{vel}}(\mathbf{k}_2) \frac{\mathbf{K} \cdot \mathbf{k}_1}{k_1^2} \frac{\mathbf{K} \cdot \mathbf{k}_2}{k_2^2} \right. \\ & \left. + b_1^L(\mathbf{k}_1) b_{\text{vel}}(\mathbf{k}_2) \frac{\mathbf{K} \cdot \mathbf{k}_2}{k_2^2} + b_1^L(\mathbf{k}_2) b_{\text{vel}}(\mathbf{k}_1) \frac{\mathbf{K} \cdot \mathbf{k}_1}{k_1^2} \right]^2 \delta_D(\mathbf{k} - \mathbf{k}_1 - \mathbf{k}_2), \end{aligned} \quad (\text{B.3})$$

with

$$G(k, \mu) \equiv \exp(-[1 + f(2 + f)\mu^2] k^2 \sigma_v^2) \quad \text{and} \quad \mathbf{K} \equiv \mathbf{k} + f(\mathbf{k} \cdot \hat{\mathbf{z}}) \hat{\mathbf{z}}, \quad (\text{B.4})$$

where σ_v was defined in equation (2.4). Before proceeding further, notice that this expression shows that the 1-loop contribution is smeared as well.

For our problem, $b_{\text{vel}}(k) = 1 - (s_0/s_1)k^2$, $b_1^L(k) = b_{10} + b_{01}(s_0/s_1)k^2$ and $b_2^L(k_1, k_2) = b_{20} + b_{21}(s_0/s_1)(k_1^2 + k_2^2) + b_{22}(s_0/s_1)^2 k_1^2 k_2^2$. This makes $b_1^L(k) + b_{\text{vel}}(k) = (b_{10} + 1) + (b_{01} - 1)(s_0/s_1)k^2$, and provides an easy way to see how the Kaiser factor in the first term on the right hand side of Eq. (B.2) is modified [62]. When multiplied by $G(k, \mu)$, the first term is the one we called ‘prop’ in the main text.

The second term is more complicated; even when there is no k -dependent bias, it generates many terms [29]. However, on the large scales most relevant to BAO analyses, the most relevant terms are those which are proportional to μ (in the square brackets above) [33]. These are generated by the fact that the initial and final pair separations will be different. If these differences are small compared to the initial separation, then a Taylor series expansion yields $\delta(\mathbf{x}) \approx \delta(\mathbf{q}) + (\mathbf{x} - \mathbf{q}) \cdot \nabla_{\mathbf{q}} \delta$. However, $\mathbf{x} - \mathbf{q} = \mathbf{S}$ is just the gradient of the gravitational potential (i.e., the force that produces the acceleration which generates the displacement).

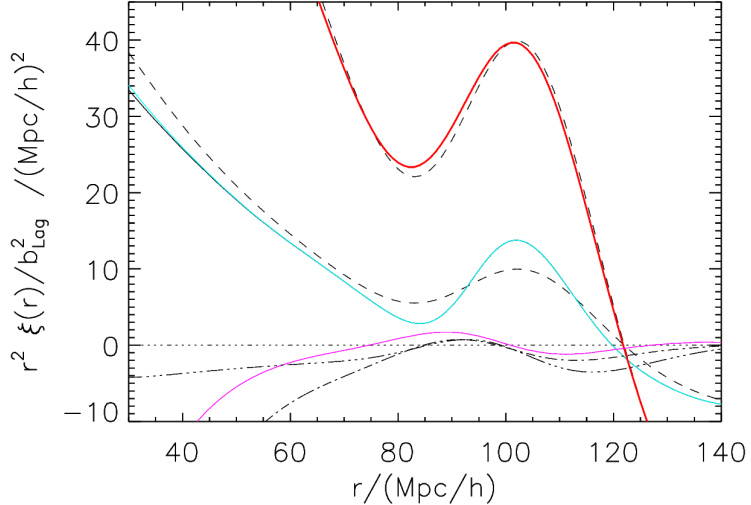


Figure 5. Evolution of the shape of the correlation function, and accuracy of our treatment of the mode coupling term. All curves have been divided by the Lagrangian bias factor b_{10}^2 . Solid cyan and red curves show the initial and Zeldovich-evolved correlation functions. Dashed curves show a smeared version of the initial shape, and this same shape multiplied by $[(b_{10}+1)/b_{10}]^2$ (i.e., $\xi_{\text{prop}}/b_{10}^2$). Solid magenta curve shows the difference between the red curve and $\xi_{\text{prop}}/b_{10}^2$, and triple-dot dashed curve shows our ξ_{MC}/b_{10}^2 with $\xi_{\text{MC}} \propto d\xi_{\text{prop}}/d\ln r$.

As a result, the second-order correlators which matter are pairwise combinations of δ^2 at one position with $\nabla\phi \cdot \nabla\delta$ at another. In configuration space, for dark matter, these correspond to the product of a logarithmic derivative of ξ_L and a volume integral of ξ_L . That product should be convolved with the Gaussian $G(k, \mu)$. (In principle, this is not the same as convolving each term and then multiplying.)

The volume integral is smoother across the BAO scale than is the derivative; we expect this to be generic. Therefore, for dark matter, we would follow CS08 in approximating the full mode coupling term as a constant times a term proportional to $d\xi_L/d\ln r$. In addition, to account for the smearing by $G(k, \mu)$, we would only smooth $d\xi_L/d\ln r$ (although we should really smooth the product of the two terms), since multiplication by a constant will not affect the smearing. How does this generalize to biased tracers?

In the main text, we approximated the full mode coupling term as a constant times a term proportional to $d\xi_{\text{prop}}/d\ln r$ (recall that ξ_{prop} denotes the smeared, k -dependent, Eulerian-biased, linear theory correlation function). This has the virtue of not requiring new parameters to specify $b_2(k)$, and would be ‘exact’ for the Lognormal Lagrangian bias model (modulo the fact that we are approximating the other term as a constant, so that the issue of smoothing is trivial).

Figure 5 shows that this works reasonably well. We assumed the tracers were initially Lognormally biased, with Lagrangian bias $b_{10} = 1$. The cyan solid line shows $r^2\xi_L/b_{10}^2$, and the red solid line shows the associated Zeldovich-evolved correlation function (also normalized by the Lagrangian b_{10}^2). The difference in amplitude is mainly driven by the fact that the bias factor evolves from b_{10} to $b_{10} + 1$; there is a secondary effect that arises from the smoothing and mainly alters the significance of the BAO feature. To illustrate, the lower dashed line shows the result of smearing the linear theory shape, and the upper dashed line shows the result of multiplying this by $[(b_{10} + 1)/b_{10}]^2$. This illustrates that the smeared linear theory,

with the Eulerian rather than Lagrangian bias factor – the quantity called ξ_{prop} in the main text – is quite a good model for the evolved correlation function. The magenta curve shows the difference between the solid red and upper dashed curves: we are interested in how well our approximation for the mode-coupling term accounts for this difference. The triple dot-dashed curve shows our approximation, and the dot-dashed curve accounts for the fact that the volume integral is not quite constant across these scales (an effect we ignore). Our approximation is quite good – especially on BAO scales.

We expect our simple parametrization of the ‘mode coupling’ term in the main text to be rather generic, especially because we expect the Zeldovich approximation – the leading order in any Lagrangian perturbation theory – to be rather generic. Moreover, if we decompose the term in square brackets into a monopole, dipole and quadrupole (for the angle between \mathbf{k}_1 and \mathbf{k}_2 , not the angle with respect to the line of sight), then all three terms have coefficient 1/2. Within GR, when one goes beyond the Zeldovich approximation, then the coefficients of the monopole and quadrupole change, but the dipole does not. I.e., moving from Zeldovich to the exact dynamics does not change the coefficient of the dipole term. Likewise, we expect that changing from GR to modified dynamics, at this order, will modify the monopole and quadrupole terms, but will leave the dipole unchanged. However, it is this dipole term which dominates the mode coupling on BAO scales, which is why we believe our treatment of mode coupling is likely to be rather general. (This dipole term arises from the fact that the displacement is the gradient of the same potential which, when inserted in the Poisson equation, yields the density. Our mode coupling term will be unrealistic if this is no longer true. See [31] for a careful discussion of how symmetries, in particular Galilean invariance, constrain LPT and ensure that, to second order, our mode-coupling term is quite general.) In any case, as the main text shows, the effects of scale-dependent bias are more important than those of mode-coupling, so we believe our simplified treatment is sufficiently accurate.